The Largest Scales in Turbulent Flow: The Structures of the Wall Layer

Javier Jiménez[1,2] and Mark Simens[1]

[1] School of Aeronautics, 28040 Madrid, Spain
[2] Centre for Turbulence Research
Stanford University, Stanford CA, 94305–3030 USA

1 Introduction

Walls are present in most flows, such as in pipes, rivers, vehicles, etc., and they profoundly influence turbulence. Wall-bounded turbulent flows are of prime technological importance, but they are also physically very interesting. We shall see that many issues in them are still not understood, and that they differ in many aspects from isotropic and homogeneous flows. They are perhaps the last area in 'classical' incompressible turbulence in which there are still open questions about basic physical mechanisms.

We will focus in this paper on the structural organization of the wall region, and specially into the genesis of the structures in the viscous and logarithmic layers. A brief review of the classical theory is given first, for the benefit of those not familiar with the subject [37,40].

To a first approximation we can assume that the flow is homogeneous in the streamwise (x) and spanwise (z) directions. In the wall-normal (y) direction the wall makes the flow inhomogeneous. It also makes it anisotropic everywhere. This is due to two effects. In the first place the impermeability condition at the wall prevents wall-normal velocity fluctuations from developing length scales much larger than y, inducing a natural scale stratification in which larger structures are only present away from the wall. Also, the wall enforces a no-slip condition for the other two velocity components, so that viscosity cannot be neglected even at high Reynolds numbers.

The flow is for these reasons governed by two different length scales. Near the wall there is a thin layer in which viscosity dominates, but in which velocities are too small compared to the free-stream velocity, U_0, for the latter to be relevant. The velocity scale is there determined by the skin friction τ as

$$u_\tau^2 = \tau/\rho = \nu \partial_y U, \tag{1}$$

where ρ is the fluid density, ν is the kinematic viscosity, and U is the mean velocity profile. The length scale is given by ν and u_τ, and variables normalized in these 'wall' units are traditionally distinguished by a $^+$ superindex. The dimensionless wall distance is, for example, $y^+ = u_\tau y/\nu$, and the dimensionless flow thickness $Re_\tau = u_\tau h/\nu$ is a good characterization of the Reynolds number of the flow. Typical values are $Re_\tau \approx 100$ for transitional flow to $Re_\tau \approx 10^4$ for

D. Reguera, L.L. Bonilla, and J.M. Rubí (Eds.): LNP 567, pp. 39–57, 2001.

geophysical ones. In this near-wall region the velocity is given by

$$U^+ = f(y^+), \tag{2}$$

where f is expected to depend only on wall properties (smoothness, etc.)

Away from the wall, where $y = O(h)$, the Reynolds number is too high for viscosity to be important. The length scale there is the flow thickness (e.g. the pipe radius), but the velocity scale for the velocity fluctuations is still u_τ. This is because momentum conservation implies that τ is transmitted more or less unchanged across the layer by the Reynolds stresses, $-\langle u'v' \rangle$. The velocity has been separated here into a mean value and fluctuations

$$\mathbf{u} = [U(y),\, 0,\, 0] + [u',\, v',\, w'], \tag{3}$$

and $\langle\rangle$ stands for temporal (or for ensemble) averaging. The streamwise, wall-normal and spanwise velocity components are u', v' and w'. The magnitude of the Reynolds stresses suggests that $u' = O(u_\tau)$ and that the velocity differences in this region are also of the same order. The general form of the velocity profile in this layer is then

$$U_0 - U = u_\tau F(y/h), \tag{4}$$

An overlap layer is needed to match the length scales in the inner and outer flows, whose ratio is $Re_\tau \gg 1$. In this layer the distance to the wall is too small for h to be relevant, $y/h \ll 1$, while the Reynolds number is too large for the viscosity to be important, $y^+ \gg 1$. The only remaining length scale is y itself, and the velocity profile can be obtained from dimensional arguments. The only possible expression for the velocity gradient is

$$\partial_y U = \frac{u_\tau}{\kappa y}, \tag{5}$$

where the empirical Kármán constant, $\kappa \approx 0.4$, is in principle universal. Integration of this differential equation yields the classical logarithmic profile

$$U^+ = \frac{1}{\kappa} \log y^+ + A. \tag{6}$$

where the constant A has to be determined independently. This additive constant controls the overall friction coefficient since, if we assume that (6) holds up to the centre of the pipe, $y = h$, we obtain u_τ in terms of A and of Re_τ. The viscous layer lies underneath the level in which (5) applies, and acts as the boundary condition which fixes A, and the drag. The empirical limits for the logarithmic layer are $y/h < 0.2$ and $y^+ > 150$ [25]

Experiments agree very well with these scaling laws [41], even if the assumptions that we have made are only true to the lowest order, and this classical theory can be safely used as a framework for the study of the wall.

2 The Balance of Turbulent Energy

There is an alternative way of understanding the structure of wall flows. Assume a streamwise-uniform flow, such as a turbulent pipe, and separate the velocity into its mean value and fluctuations. We can write an equation for the evolution of the mean turbulent kinetic energy, $K = \langle u'^2 + v'^2 + w'^2 \rangle / 2$,

$$\partial_y \Phi_T = -\langle u'v' \rangle \partial_y U - \varepsilon + \nu \, \partial_{yy} K. \tag{7}$$

In this equation the first term in the right-hand side is the production of turbulent energy by the interaction between the mean shear and the Reynolds stresses, the last one is the large-scale viscous diffusion of the kinetic energy, which can be neglected everywhere except in the viscous sublayer, and ε is the dissipation by the small scales $\nu \langle |\nabla \mathbf{u}|^2 | \rangle$. The balance of these three terms is compensated in the left-hand side by the divergence of a spatial energy flux

$$\Phi_T = \frac{1}{2} \left\langle v' (u'^2 + v'^2 + w'^2) \right\rangle + \langle v' p' \rangle, \tag{8}$$

where p' are the pressure fluctuations.

This equation provides an alternative derivation of the logarithmic velocity profile [40, p. 135]. If we assume that the energy production and dissipation are in equilibrium within the logarithmic region, and take the latter to be $u_\tau^3 / \kappa y$, the energy balance becomes,

$$u_\tau^2 \partial_y U = u_\tau^3 / \kappa y, \tag{9}$$

which integrates directly to (6). The left-half side of this equation is an exact expression for the energy production, while the right-hand side depends only on generic properties of the turbulent cascade. The assumption is that the cascade is implemented by approximately isotropic eddies whose velocities are $O(u_\tau)$ and whose sizes are $O(y)$. Note that this assumption is equivalent to the length scaling hypothesis used to derive (6), but that here it gives a more concrete interpretation of the Kármán constant κ as defining the integral scale of the eddies of the logarithmic region.

A consequence of this analysis is that the energy flux Φ_T should be constant across the logarithmic layer, and this is tested in figure 1.a, which contains data from three numerical channels at moderate Reynolds numbers. Positives fluxes flow away from the wall, and an increase of the flux with y implies a local excess of energy production. The three curves collapse well near the wall, where energy production dominates. Part of the excess energy diffuses into the wall, but the rest flows through the logarithmic layer into the outer flow, where dissipation is dominant. In this sense, the wall provides the power needed to maintain turbulence in the outer region. There is a plateau in the logarithmic region, in agreement with (9), together with perhaps a second energy production peak near the outer edge of the logarithmic layer.

It is unfortunately difficult to measure all the terms of the energy equation in experimental flows, and there are no data equivalent to those in figure 1**(a)** at

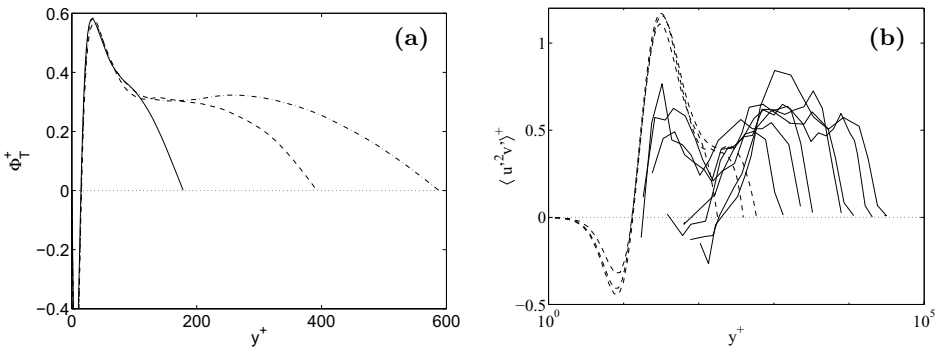

Fig. 1. Spatial flux of turbulent energy in wall bounded flows, normalized by u_τ^3. **(a)** Total flux computed from integrating equation (7) in numerical plane channels. ——— , $Re_\tau = 180$ [20]; – – – – , $Re_\tau = 395$; —·— , $Re_\tau = 590$ [27]. **(b)** Flux of streamwise turbulent fluctuations. The dashed lines are the three channels in **(a)**. The solid ones are boundary layers from [8]. $Re_\tau \approx 1,200 - 3 \times 10^4$.

higher Reynolds numbers. Some parts of Φ_T have however been measured and can be used to check how representative are the numerical results. This is done in figure 1**(b)**, which shows the turbulent transfer of streamwise fluctuations, $\langle u'^2 v' \rangle$, which accounts for about half of the flux in (8). That figure includes the numerical channels and experimental boundary layers at much higher Reynolds numbers. Notwithstanding the uncertainties in the experimental data, specially where the probe length is comparable to the wall distance, both set of measurements coincide where they overlap, giving some confidence on the conclusions from the numerics.

The picture suggested by this discussion is that of an energy producing region near the wall ($y^+ < 50$), which exports some of its extra turbulent energy across the logarithmic region into the outer flow. This spatial energy transport is an energy cascade different from the usual Kolmogorov one. In the latter, energy generated at some place is transferred locally to the smaller scales, where it is eventually dissipated by viscosity. In the spatial cascade the energy is not dissipated locally, but is transferred to other locations where it is eventually dissipated by cascading to smaller scales.

This second cascade is only found in inhomogeneous flows, and does not involve dissipation. In fact, since we have seen that in wall turbulence it flows away from the wall, where the scales are larger, it is actually a reverse cascade. Both the spatial and the Kolmogorov cascades are present in wall flows. It is difficult to compare their magnitude since Φ_T, which is an energy flux per unit area, has different units from ε, which is a flux per unit volume. We can however form a length from the two quantities, $\lambda_T = \Phi_T / \varepsilon$, which is the thickness of the layer over which the Kolmogorov cascade would be able to dissipate all the energy provided by the spatial flux. It follows from figure 1**(a)**, and from the estimates in (9), that $\lambda_T \approx 0.15y$, so that the turbulent energy being transferred

through each level of the logarithmic layer is equivalent to the energy being generated in the top 15% of its distance to the wall.

3 The Near-Wall Region

Because of this energy-generating property, and because we have seen that the magnitude of wall drag is controlled there, the region below $y^+ \approx 100$ has been the subject of intensive study. In this layer the wall-normal Reynolds numbers are low, and we may expect quasi-laminar structures whose behaviour can be understood deterministically. In some sense this region corresponds to the Kolmogorov viscous range of isotropic turbulence, and it is easy to show that the Kolmogorov and the wall-unit length scales are identical.

The dominant structures in this region are streamwise velocity streaks and quasi-streamwise vortices. The former were the first ones to be recognised [19], and consist of long ($x^+ \approx 1000$) sinuous arrays of alternating streamwise jets superimposed on the mean shear, with an average spanwise separation $z^+ \approx 100$ [33]. At the spanwise locations where the jets point forward, the wall shear is higher than the average, while the opposite is true for the 'low velocity' streaks where the jets point backwards. The net effect is to increase the mean wall shear, and it is the immediate cause of the turbulent wall drag [28]. Many attempts to control drag have therefore centred on weakening these near-wall structures [5,14].

The quasi-streamwise vortices are slightly tilted away from the wall, and each one stays in the near-wall region only for $x^+ \approx 200$ [13]. Several vortices are associated with each streak, with a longitudinal spacing of the order of $x^+ \approx 400$ [16]. Some of them are connected to the trailing legs of the vortex hairpins of the outer part of the boundary layer [29], but most merge into disorganised vorticity after leaving the immediate wall neighbourhood [32].

It has long been recognised that the vortices cause the streaks by advecting the mean velocity gradient [3]. This process is independent of the presence of the wall, as shown by the observation in [24] of streaks in uniformly sheared flows.

There is less agreement on the mechanism by which the vortices are generated. It was already proposed in [19] that streaks and vortices were part of a cycle, in which the latter were the result of an instability of the former. The argument was made more specific by [34], who noted that the spanwise velocity gradients that separate the low- from the high-velocity streaks are subject to inflectional instabilities. This conceptual model has been elaborated and used to explain several properties of disturbed boundary layers by [14,12] among others, and is the essence of the quasilinear models developed at MIT and Cornell, and reviewed in [22,10]. It can be summarised as that the quasi-streamwise vortices act on the mean shear to create the streaks, which become inviscidly unstable and eventually produce tilted streamwise vortices.

A slightly different point of view is that the cycle is organized around a nonlinear travelling wave, which would represent a permanently disturbed streak. This is not so different from the previous instability model, which essentially

assumes that the undisturbed streak is a fixed point, and that the cycle is a homoclinic orbit running through it. Candidate nonlinear waves have been computed by [36] and others, and identified as part of a particular path to turbulent transition in [38]. Finally, reduced models based on this approach have been formulated in [35]. A difficulty with most of these studies is that there is no clear connection between the object being identified and full-scale turbulence. What is needed is a demonstration that a turbulent flow can be continuously modified into one of these reduced objects while still remaining identifiably turbulent.

A possible way of doing this was proposed by [16], who substituted a full turbulent channel with an array of identical computational boxes, periodic in x and z, but each with its full wall-normal extent. The idea was to substitute the complexity of all the mutually interacting turbulent units near the wall by a 'crystal' of identical structures, all of them executing synchronously the turbulence regeneration cycle. The 'unit cell' of the crystal was adjusted to the smallest dimension that would maintain turbulence, which turned out to contain a single wavelength of a velocity streak and a pair of quasi-streamwise vortices. These structures went through a complex cycle which was still difficult to analyze, and the statistics of the fluctuations were essentially identical to those of fully developed channels. This 'minimal' system has often been used as a surrogate for real wall turbulence, and most of the reduced models mentioned in the last paragraph actually refer to it.

The previous experiment eliminated the possibility that wall turbulence required the interaction between neighbouring wall structures, but did nothing about the interaction with the core flow, which was still present. The question of the necessity of inner-outer interaction in wall turbulence has been a matter of much discussion. It is important in formulating scaling laws for the different regions, and in deciding which parts of the flow to target when designing turbulence control strategies.

An important step in clarifying this question was taken by [17], who eliminated the vorticity fluctuation in the outer flow of a numerical channel by using a numerical filter which acted as a variable viscosity, low near the wall and high outside. They were able to show that the wall cycle was 'autonomous' in the sense that it could run independently of the outer flow as long as it was not filtered below $y^+ \approx 60$. Again the statistics were similar to those of full turbulence.

The experiment of running a system that is both 'minimal', in the sense that its wall-parallel size is small enough to contain a single copy of the structures, and 'autonomous' in the sense of having no outer flow, requires some care, and had not been achieved until now. Some preliminary results are discussed next.

In all the numerical experiments the vertical filter was set to $y^+ = 50$, and the wall was run until it achieved statistically steady state. Tests were run with progressively smaller wall-parallel wavelengths, until enough flow simplification was achieved. This happened with for $x^+ \times z^+ = 500 \times 220$, which is somewhat longer and somewhat wider than the minimal unit. The flow entered a regular limit cycle, as opposed to the chaotic behaviour characteristic of full, or even of minimal full-depth channels. Decreasing the box side made the cycle weaker and

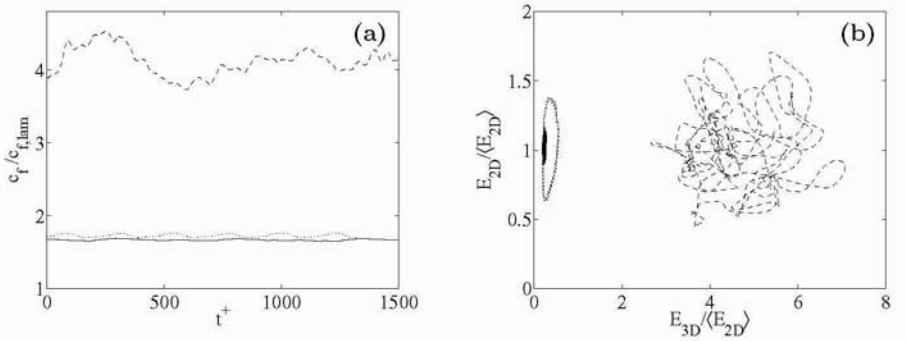

Fig. 2. Numerical experiments on minimal autonomous walls. – – – – , full-depth channel, $x^+ \times y^+ \times z^+ = 770 \times 380 \times 340$; ····· , $500 \times 50 \times 220$; ——— , $300 \times 50 \times 180$. All cases are shown after reaching statistically steady state. (**a**) Friction coefficients compared with the theoretical laminar value. (**b**) Perturbation energies defined in the text. There are seven cycles in the dotted line.

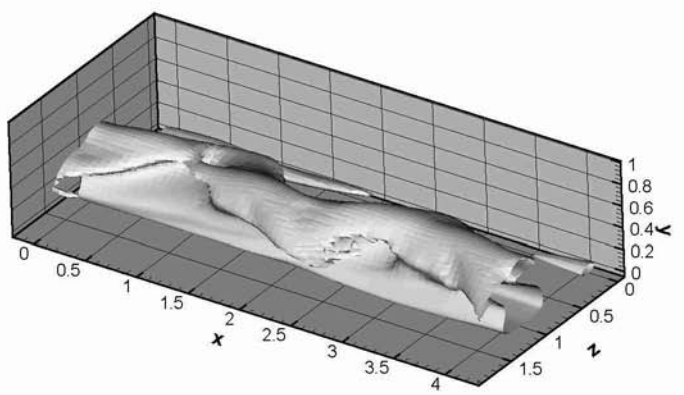

Fig. 3. Isosurface of the streamwise perturbation velocity for the intermediate box in figure 2. $u'^+ = -1$. Flow is from left to right.

drove it almost to a permanent travelling wave. The time evolution of the friction coefficients of two such boxes is shown in figure 2(**a**), which also contains data from a full-depth channel for comparison. Figure 2(**b**) shows the same data in a different representation. Orbits are shown in terms of the two-dimensional and three-dimensional energy of the v' fluctuations, as first used in [38]. The former is the energy of the fluctuations of the streamwise-averaged flow, and therefore represents the intensity of long objects, essentially streaks. The three-dimensional component contains the deviations from streamwise uniformity. The figure underscores the difference between the limit cycle and the chaotic evolution of the full channel, and shows that the simplification process in constrained systems corresponds to a decrease of the three-dimensionality of the flow. In agreement with this, and with previous results in [16,17], the fluctuation intensity profiles

for these flows are essentially normal for the streamwise velocity component, but weaker than normal for the other two components.

A three-dimensional representation of the streak in the longer of the two autonomous boxes of the previous figure is shown in figure 3. It shows a streak with two waves, associated to each of which there is a pair of quasi-streamwise vortices (not shown). During the turbulent cycle these waves grow deeper and shallower, but the streak is never uniformly straight. The presence of two waves suggests that it should be possible to have an autonomous flow with a single one, and the shorter box in figure 2 is indeed one such solution. Even if the present flows are not permanent waves, they are very weakly oscillating ones, and it should be emphasized that they are statitistically stationary and autonomous, in the sense that there are no other vorticity fluctuations in the numerical box except those seen in the figure. They have also been derived from a fully turbulent flow by a continuous set of transformations in which their statistical properties were either maintained or evolved smoothly. They are the best representation that we have up to now of the elemental 'engine' which powers near-wall turbulence.

Figure 3 is qualitatively very similar to the traveling wave obtained in [36], and to the structures educed from larger channels by [16,17]. Casual observation of the differences between these and larger flows suggest the root of the complexity in the latter. As the streak goes through the cycle, it ejects some vorticity into the outer flow, essentially as a small hairpin vortex. In full-depth flows this vorticity evolves, becomes disorganized, and eventually comes back to modify the next cycle of the streak. In autonomous flows the vorticity is damped by the filter as soon as it is ejected, and this randomizing mechanism is not present.

4 The Structures of the Overlap Layer

Although the structures of the near-wall region have been the subject of a lot of work, the overlap layer has been studied mostly from the statistical point of view. The reason has been in part that it is difficult to obtain experimentally flows with a clean overlap region. If we follow the criterion that the latter exists only above $y^+ \approx 100 - 200$ and below $y/\delta \approx 0.15 - 0.2$, the minimum Reynolds number for which some overlap can be expected is $Re_\tau = 500$, and at least $Re_\tau = 1000$ is needed to have some confidence in the results. Most structural studies, which typically require visualizations and measurements over extended regions, are made at lower Reynolds numbers. This is also true of numerical simulations. Moreover, even if the Reynolds number is high enough, the overlap structures are large and themselves turbulent. This makes them harder to visualize, and even to define, than the smoother ones near the wall.

Most of the information on this region comes from velocity spectra, and suggests the presence of extremely large structures [4,7,30]. A compilation of premultiplied spectra of the streamwise velocity fluctuations, $k_x E_{uu}(k_x)$, is given in figure 4**(a)**, and they extend to wavelengths, $\lambda = 2\pi/k$, of the order of $60 - 100y$. At the edge of the overlap region, this corresponds to $15 - 20$ times the boundary layer thickness. This long-wave k_x^{-1} energy spectrum of wall flows has

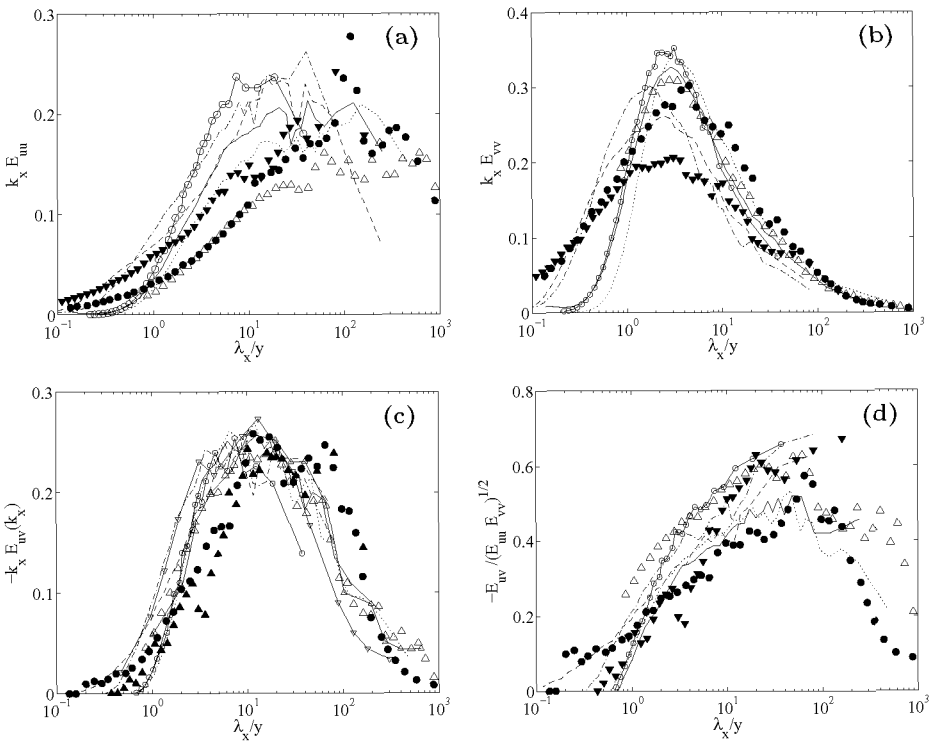

Fig. 4. Premultiplied velocity spectra, as a function of streamwise wavelength $\lambda_x = 2\pi/k_x$, normalized to integrate to unity. Abscissae are normalized with wall distance. **(a)** E_{uu}. **(b)** E_{vv}. **(c)** $-E_{uv}$. **(d)** Structure cross-correlation parameter $-E_{uv}/(E_{uu}E_{vv})^{1/2}$. —○— , numerical channel, $u_\tau\delta/\nu = 590$, $y^+ = 100$ [27]. —△— , $y^+ = 100$; —▽— , $y^+ = 250$, pipe with $u_\tau R/\nu = 2100$ [23]. Simple lines are laboratory smooth-wall boundary layers from Carlier (private commun.): ····· , $y^+ = 95$; - - - - , $y^+ = 360$. $u_\tau\delta/\nu = 2530$. ——— , $y^+ = 110$; —·— , $y^+ = 970$. $u_\tau\delta/\nu = 7050$; Symbols are from the atmospheric boundary layers: △ , $y/h = 100$; • , $y/h = 1000$; from [11], $U \approx 10$ m/s at 10 m, and roughness height, $u_\tau h/\nu \approx 400$. If we assume the boundary layer thickness to be $\delta \approx 500$ m, $\delta^+ = \delta/h \approx 5 \times 10^4$. ▼ , from [1] $y = 1.7$ m, $U = 6.2$ m/s, and roughness height, $h = 4$ mm.

been extensively studied in [29], and is only present at wall distances which more or less coincide with the overlap layer. Since the total energy of the fluctuations can be written as

$$\langle u^2 \rangle = \int_0^\infty k_x E_{uu}(k_x)\, \mathrm{d}\log\lambda_x, \tag{10}$$

premultiplied spectra extending to long wavelengths imply that a large fraction of the total fluctuating kinetic energy is associated with those structures.

Even if most of this information has been available for some time, it was not until the compilations presented in [15,21], or until the publication of the thesis [9] that the real size of these structures became widely realized. A consequence

has been that many experimental measurements, and most computations, were not planned with these structures in mind, and that the records compiled in many of them are too short, giving the false impression that the structures are shorter than they really are.

A compilation of spectra for the wall-normal velocity component is also given in figure 4, which emphasizes the paucity of available data for E_{vv} and for the E_{uv} cospectrum. The latter is specially important, since its integral is the transverse Reynolds stress $-\langle u'v' \rangle$, which in turn determines the mean velocity profile. Only if this quantity scales well with the distance to the wall is there any reason to expect the self-similar scaling of the Reynolds stresses which is needed for the logarithmic law. It is seen in figures 4 that the E_{vv} and E_{uv} spectra actually scale better with wall distance than E_{uu}. This is especially true for the cospectrum, even if the experiments used in the figure are very different from each other, giving strong support to the logarithmic velocity profile. Older compilations of stress cospectra for more homogeneous conditions can be found in [26,2].

It is interesting that the wavelengths implied by the spectra for the Reynolds stresses are longer than those the wall-normal velocity, even if the former, $-\langle u'v' \rangle$, cannot exist without the latter. The reason is clarified by the spectral distribution of the structure parameter in figure 4**(d)**, which describes the *efficiency* of the turbulent fluctuations in transporting momentum. If this quantity is low, the u and v fluctuations are uncorrelated, and only produce low stresses, while the opposite is true if it is high. The distribution in figure 4**(d)** is consistent with the intuitive idea that isotropic turbulence is unable to transmit momentum. For wavelengths $\lambda_x \approx y$ the efficiency parameter is almost zero, since these scales are small enough not to be influenced by the wall, and are therefore almost isotropic. It is only for the longer structures, which feel the wall and the mean shear, that the efficiency approaches unity and that the Reynolds stresses become significant. It is this bias of the efficiency towards longer wavelengths that shifts the peak of the cospectrum with respect to that of E_{vv}.

Much less is known of the spanwise extent of these fluctuations. The spectra in figure 5 suggest that both u and v have lateral wavelengths which are low multiples of the distance to the wall, but they were compiled from numerical simulations at low Reynolds numbers where a proper logarithmic layer does not exist. They also correspond to computational boxes that, as we have noted above, are too short to contain the longest streamwise wavelengths, and it is possible that those long waves may also be wide, in which case they would be missed by the numerical spectra. This is suggested by the two-dimensional spectra in figure 6, which correspond to the same numerical data, and which show a 'diagonal' trend for both E_{uu} and E_{ww}, suggesting that longer and wider structures could be present in larger numerical boxes. To our knowledge there are no published experimental spanwise spectra on which to check this possibility, but there is at least one report, from the analysis of PIV data in a turbulent channel, which claims that most of the energy in E_{uu} very close to the wall is in very wide spanwise wavelengths [39].

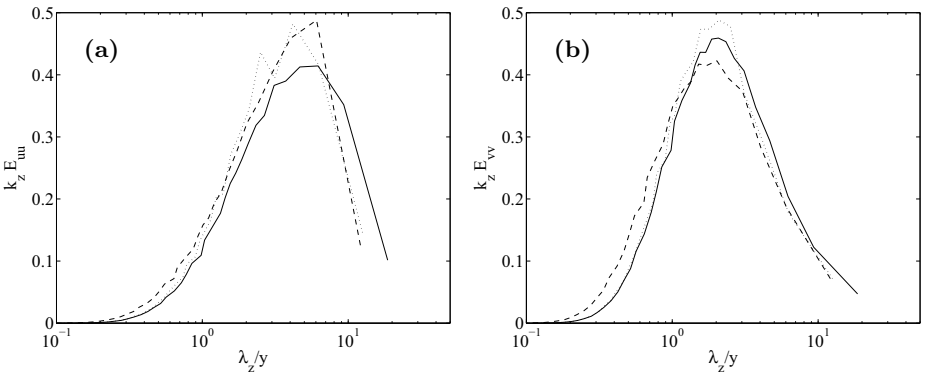

Fig. 5. Premultiplied velocity spectra, as a function of spanwise wavelength $\lambda_z = 2\pi/k_z$, normalized to integrate to unity. Abscissae are normalized with wall distance. Numerical channel with $Re_\tau = 590$, ——— , $y^+ = 100$; - - - - , $y^+ = 150$; ····· , $y^+ = 100$ at $u_\tau\delta/\nu = 395$ [27]. **(a)** E_{uu}. **(b)** E_{vv}.

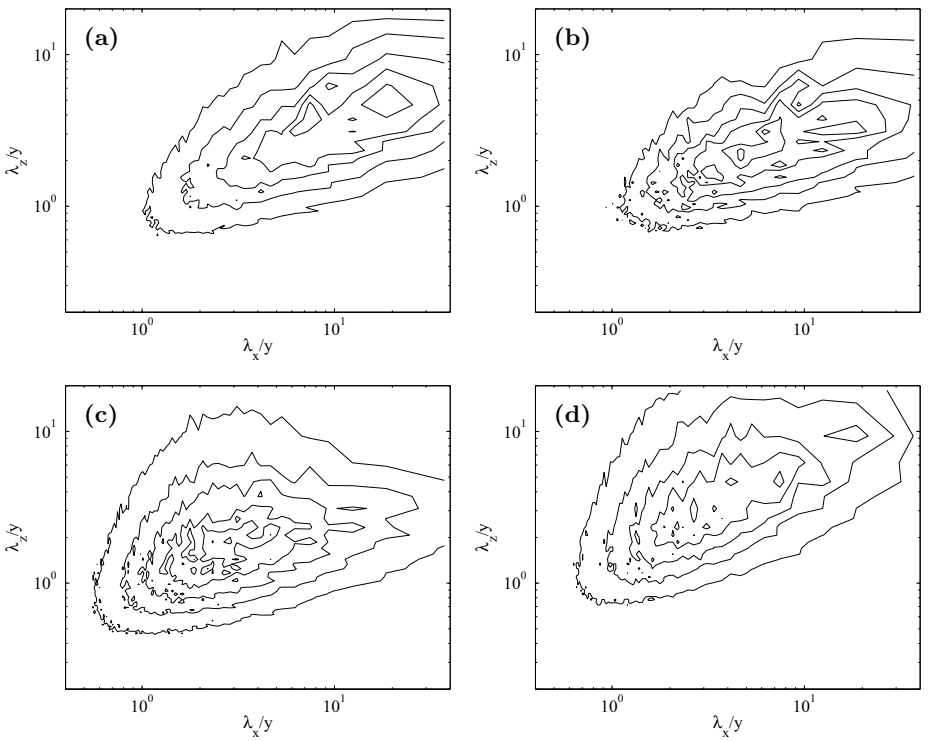

Fig. 6. Premultiplied two-dimensional velocity spectra, normalized to integrate to unity, as a function of the streamwise and spanwise wavelengths normalized with wall distance. Numerical channel from [27]. $Re_\tau = 590$, $y^+ = 100$. **(a)** E_{uu}. **(b)** $-E_{uv}$. **(c)** E_{vv}. **(d)** E_{ww}. Contour intervals are 0.01 (0.01) for E_{uu}, and 0.03 (0.03) for the other three spectra.

From the evidence of the spectra in this section, at least until the issue of the spanwise wavelengths is clarified, the geometry of the large structures of the overlap layer is that of long and narrow regions which exist only for the streamwise, but not for the wall-normal, velocity component, and which can therefore be described as streaks, broadly similar to those of the near-wall region. They are however much larger than the latter, and fully turbulent rather than laminar or transitional. Some references to direct observations of these large streaky structures, in nature and in numerical simulations, can be found in [15].

5 Linear Stability of the Mean Velocity Profile

The size of the structures discussed in the previous section suggests that they should be describable in terms of linear processes. Since we have observed that they contain much of the kinetic energy, which is of the order of u_τ^2, their characteristic velocity scale is u_τ, and their turnover time is $T_L = L/u_\tau$, where L is their characteristic length. This self-deformation time competes with the shearing time scale of the mean velocity profile which, from the logarithmic law, is $T_s = (\partial_y U)^{-1} = \kappa y/u_\tau$. For any structure for which $L \gg y$, including most of those discussed in the previous section, T_L is much slower than T_s, and the nonlinear self-interactions are not relevant for the dynamics.

The traditional emphasis when analyzing linear structures has been on unstable eigenmodes, since it is clear that, if they exist, they will grow and be observed. These are commonly associated with inflection points of the mean profile [6], in which case their growth rates are of the order of the local shear, and they compete with other processes present in the turbulent flow.

The mean velocity profiles of most attached wall flows have no inflection points, and are believed to be stable. This was shown for example in [31] for a turbulent channel with impermeable walls. They used a model velocity profile which approximated those of experimental channels, and substituted the molecular viscosity by the isotropic eddy viscosity which was needed to maintain the profile. Both approximations need some comment. The first one assumes that something like a mean profile exists instantaneously, which is known not to be the case. The second one assumes that the Reynolds stresses are carried by structures which are much smaller than those being studied. In both cases the implicit assumption is that there is a separation of scales between the large structures and the 'small scale' turbulence.

Such spectral gaps do not generally exist, since turbulent spectra are broadbanded, and such assumptions have to be justified in each particular case. There are two reasons why we will use it here. In the first place, and as long as we restrict ourselves to analyzing the very long u structures, the spectra in the previous section suggest that the Reynolds-stress producing scales are indeed shorter by an order of magnitude, allowing us to plausibly model them by an isotropic eddy viscosity. Note that this argument would not be true for the v structures, whose spectral peaks are at shorter wavelengths than those of E_{uv}. This suggest that we should use the mean-field, eddy-viscosity approximation,

estimate from it the Reynolds stresses, and use only results for those wavelengths which are clearly longer than the stress-producing ones.

The second reason for using this approximation is that we shall see that the eigenfunctions of interest are essentially neutral inviscid modes, and that the role of the eddy viscosity is to damp them slightly. We may therefore expect the eigenfunctions to be essentially correct even if the magnitude of the imaginary damping part of the eigenvalue is not accurate.

With these limitations in mind we will next analyze the stability of wall flows using linear perturbations of the mean profile, and substituting the constant molecular viscosity by the variable isotropic eddy viscosity,

$$\nu_t = u_\tau^2 \, \frac{1 - y/h}{\partial_y U}. \tag{11}$$

Note that this definition of ν_t includes the molecular viscosity. Assume perturbation velocities of the form

$$v' = \widehat{v}(y) \exp \mathrm{i}[\alpha_1 (x - ct) + \alpha_3 z], \qquad \text{etc.}, \tag{12}$$

where the wavenumbers α_1 and α_3 are real, and c is an unknown phase velocity, possibly complex. The linearized equation takes the form

$$(U - c)\,(\partial_{yy} - \overline{\alpha}^2)\,\widehat{v} - U_{yy}\widehat{v} + \mathrm{i}\alpha_1^{-1}(\partial_{yy} - \overline{\alpha}^2)[\nu_t(\partial_{yy} - \overline{\alpha}^2)\,\widehat{v}] = -\mathrm{i}\alpha_1 \nu_{t,yy}\widehat{v}, \tag{13}$$

where $\overline{\alpha}^2 = \alpha_1^2 + \alpha_3^2$, and the subindices of the mean velocity and eddy viscosity denote derivatives with respect to y. The left-hand side is the standard Orr-Sommerfeld stability equation [6], while the extra term in the right-hand side originates from the variation of the eddy viscosity, and can be shown numerically to affect the solutions only slightly. The no-slip boundary condition can be written, using continuity, as

$$\partial_y \widehat{v}(2h) = \partial_y \widehat{v}(0) = 0, \tag{14}$$

while the impermeability condition is

$$\widehat{v}(2h) = \widehat{v}(0) = 0. \tag{15}$$

We will substitute it here, for reasons that will later become clear, by the more general form,

$$\widehat{v} + \beta_0 \widehat{v} + \beta_1 \partial_y \widehat{v} = 0, \tag{16}$$

where β_0 and β_1 are arbitrary small parameters.

Except for the right-hand side of (13), Squire's transformation [6] reduces the problem (13)–(15) to a two-dimensional one with $\alpha_3 = 0$, and a modified viscosity

$$\widehat{\nu}_t = \overline{\alpha} \nu_t / \alpha_1, \tag{17}$$

Oblique waves therefore behave as normal ones with the same $\overline{\alpha}$ and higher viscosity and, since the latter is generally a stabilizing effect, we may assume

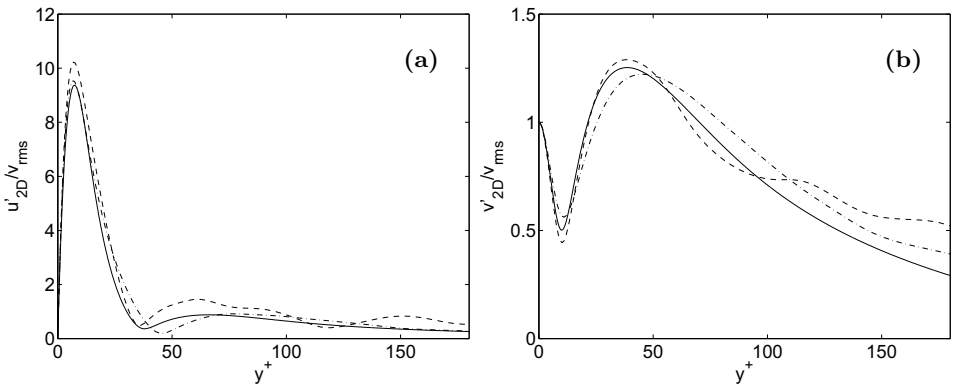

Fig. 7. Profiles of the spanwise-coherent fluctuation intensities, normalized with the forcing v_{rms} at the wall. Phase velocity of the forcing $U_c^+ = 10$. Wavelength $\lambda_x/h = 2.7$. $h^+ \approx 200$. - - - - , $v_{rms}^+ = 0.1$; —·— , $v_{rms}^+ = 0.2$; ——— , linear calculation. **(a)** $\langle u^2 \rangle^{1/2}$. **(b)** $\langle v^2 \rangle^{1/2}$.

for the moment that $\alpha_3 = 0$. The right-hand side of (13) does not transform correctly under (17), so that the transformation is not exact, but we have seen that its effect is small.

The accuracy of the eddy-viscosity approximation can be tested by forcing experiments in which a sine-wave transpiration is artificially imposed in one of the walls. This is equivalent to substituting (15) by $\widehat{v}(0) = 1$. The result, compared with direct simulations of forced turbulent channels, is shown in figure 7, which is adapted from [18]. The linear scaling of the velocity perturbation profiles is excellent for two different forcing intensities, and so is the agreement with linear theory, even if the forcing in the simulations was strong enough to change the magnitude of the skin friction by almost 40%. Other quantities are however not well predicted. The increment of the Reynolds stresses due to the forcing is, for example, underpredicted by a factor of about two.

5.1 A Simple Inviscid Profile

The general properties of the stability problem can best be understood by the inviscid analysis of a piecewise-linear velocity profile over a single wall,

$$U = U_0 y/h \quad \text{if} \quad y < h; \qquad U = U_0 \quad \text{otherwise.} \tag{18}$$

In the inviscid case (13) reduces to a second-order equation, and the only boundary conditions are the generalized impermeability condition (16) at the wall, and $\widehat{v} \to 0$ as $y \to \infty$. The no-slip condition is lost. The solution is continuous everywhere and can be expressed as a combination of exponentials $\exp(\pm \overline{a} y)$. The discontinuity of $\partial_y \widehat{v}$ at $y = h$ is computed by integrating (13) across the corner of the profile. There is a single eigenvalue which can be expressed as a function of the wavenumber magnitude, $\overline{\alpha}$, and of the permeabilities.

In the impermeable case, $\beta_0 = \beta_1 = 0$, the eigenvalue is neutral. The phase velocity is real and equal to

$$c_r/U_0 = \left(\mathrm{e}^{-2\overline{\alpha}h} + 2\overline{\alpha}h - 1\right)/2\overline{\alpha}h. \tag{19}$$

For very long waves $c_r/U_0 \approx \overline{\alpha}h \ll 1$, and the corresponding eigenfunctions decay only slowly at large y. For short waves, $\overline{\alpha}h \gg 1$, the phase velocity is $c_r \approx U$, and the eigenfunctions are localized in the neighbourhood of the corner of the profile. This mode corresponds to a neutral shear wave, and exists for all boundary layer profiles in the inviscid limit. Viscosity weakly damps it, but it is always there, potentially ready to couple with the permeability boundary condition (16).

For $\beta_i \ll 1$ we can indeed expand the eigenvalues as a series of the boundary condition coefficients. The lowest order correction is linear in β

$$\Delta c/U_0 = \beta_1 \mathrm{e}^{-2\overline{\alpha}h}/h. \tag{20}$$

The change in the real part of the phase velocity is $O(\beta)$ and can be neglected to the lowest order, but the stability is determined by the imaginary part of β_1. The unstable eigenfunctions are also $O(\beta)$ perturbations of the neutral mode of the homogeneous boundary conditions.

5.2 An Example: The Porous Wall

A direct application of the previous stability analysis was found in the numerical experiments of turbulence over porous walls carried out in [18]. The porosity of the wall is modelled by a Darcy-type law

$$v' = -\gamma p', \tag{21}$$

where γ is a porosity coefficient with dimensions of an inverse velocity. It is zero for impermeable walls, and tends to infinity for completely permeable ones.

The pressure at the wall is given by

$$\overline{\alpha}^2 \widehat{p} = \partial_y[\nu_t(\partial_{yy} - \overline{\alpha}^2)\widehat{v}] + \mathrm{i}\alpha_1 \left(U_y \widehat{v} + c\partial_y \widehat{v}\right). \tag{22}$$

In the inviscid case (21) has therefore the general form (16) with $\beta_1 = \mathrm{i}\gamma\alpha_1 c_r/\overline{\alpha}^2$, where c_r can, to lowest order, be substituted by (19). Since the imaginary part of β_1 is positive, its effect is destabilizing and we expect large-scale instabilities, which were observed. The predicted growth rate for low porosities is

$$\alpha_1 \Im(c) h/U_0 = \gamma \alpha_1^2/\overline{\alpha}^2 c_r. \tag{23}$$

The ratio of the wavenumbers is maximum when $\alpha_3 = 0$, and we therefore expect to observe, as we do, spanwise oriented perturbations.

There is in this case a simple interpretation for the observed instability. When $\gamma U_0 \gg 1$ the porous boundary condition (21) is equivalent to $\widehat{p}(0) = 0$ which, using (22), reduces to $\partial_y \widehat{v}(0) = 0$. If we extend antisymmetrically the profile

(18) to $y < 0$, it becomes a piecewise-linear free shear layer, whose stability characteristics are well known (see [6, p. 146]). The boundary condition at $y = 0$ fixes the parity of the solution. The $\widehat{v}$ eigenfunctions of the infinite-porosity case are even with respect to $y = 0$, inducing sinuous deformations of the shear layer. These are the well-known Kelvin-Helmholtz instability waves, and they are the only instabilities of this profile. The varicose deformation generated by the impermeable boundary condition, $\widehat{v}(0) = 0$, is neutral. The intermediate porosities connect the Kelvin-Helmholtz instability of the fully permeable wall to the varicose neutral modes of the impermeable one.

A word of caution is needed here. The previous inviscid analysis of a model boundary layer can be repeated for a channel [18], and the results are somewhat different. There are in that case two initially neutral modes, which agree for short wavelengths, but which differ substantially for long ones, suggesting that the stability characteristics of internal and external flows might not be exactly equal in that limit.

5.3 Viscous Modes

The important conclusion that can be drawn from the previous discussion is that there are weakly damped eigenfunctions of the mean velocity profile of wall-bounded turbulent flows which can become unstable by coupling to a transpiration at the wall. The details of that coupling control the growth rate of the instability, but are relatively unimportant in determining the structure of the eigenfunctions, which are always small perturbations of the neutral inviscid ones.

There is an aspect in which this is not true. The inviscid eigenfunctions depend only of the magnitude $\overline{\alpha}$ of the wavenumber, since the difference between spanwise and oblique waves can be absorbed in Squire's transformation (17). Which wavevector is chosen depends on the transformation properties of the boundary condition (16). We saw for example that in the porous case the boundary condition selects spanwise waves, but other couplings can result in predominantly streamwise, or in essentially isotropic, perturbations. The vertical structure is, on the other hand, only weakly dependent on this.

An intriguing possibility is that the large scales of the logarithmic layer could be explained by such an instability, in which the coupling would be with the active oscillators of the near-wall region. Physically we would be speaking of an interaction between the large outer scales and the near-wall bursting cycle. Although we have seen that the latter can run autonomously, without input from the outer flow, it is probable that it can be modulated by it. The inner layer would, in this view, provide a transpiration boundary condition for the outer one.

Although a lot of work is needed before this conjecture can be tested, there are some hopeful indications. The full eigenvalue problem (13), with homogeneous boundary conditions, can be solved numerically for the mean profile of the $Re_\tau = 590$ channel in [27]. The result is a set of eigenfunctions which depend, assuming $\alpha_3 = 0$, on the streamwise wavelength $2\pi/\alpha_1$. As one would

expect, the eigenfunctions corresponding to short wavelengths are concentrated near the wall and are strongly damped. Longer eigenfunctions penetrate deeper, move faster, and are only weakly damped.

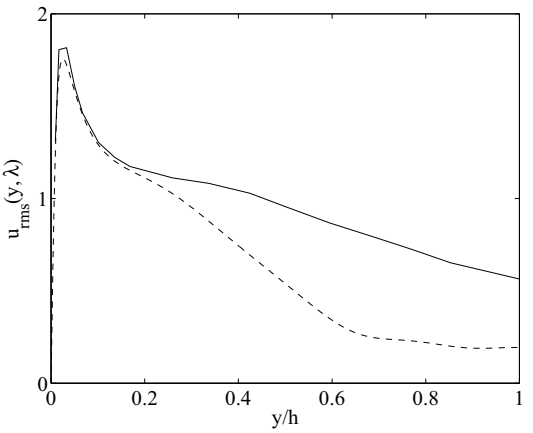

Fig. 8. Fluctuation intensity profiles for the streamwise velocity fluctuations for a wavenumber $k_x/h = 2\pi$. ——— , from the one-dimensional spectra in the channel simulations in [27]; – – – – , from the eigenfunctions of (13). $Re_\tau = 590$. The amplitude scale is arbitrary in both cases.

Since we have energy spectra for the numerical flow in [27], we can compute how the energy contained in a given set of wavelengths depends on the distance to the wall, and compare it to the absolute value of the eigenfunction. They should have similar structures. This is done in figure 8 for $\lambda_x/h = 2\pi$, which is the longest one available in the simulation. They agree fairly well in the logarithmic and wall layers, $y/h < 0.2$, although, given the many approximations involved, this should only be taken as indicative.

5.4 Conclusions

We have reviewed some of the open problems in the physics of the near-wall and logarithmic layers of wall flows. We have seen that the former is an active site for turbulence generation, which can run autonomously and which exports energy to the rest of the flow.

Its structure is reasonably well described in terms of a regeneration cycle involving long streamwise velocity streaks and shorter quasi-streamwise vortices. The cycle seems to be associated to a nonlinear structure, a wavy streak, which has been identified theoretically and observationally, and which we have shown here to be self-sustaining in a severely truncated numerical experiment.

Farther from the wall the structures become larger, with lengths which are much longer than the flow thickness. Even so their spectra scale well with wall

distance, specially for the wall-normal components. We have shown some circumstantial evidence that these very large scales correspond to linear eigenfunctions of the mean velocity profile, weakly damped for homogeneous boundary conditions, but destabilized by their interaction with the active near-wall turbulence cycle.

This work was supported in part by the Spanish CICYT contract PB95-0159, by ONR grant N0014-00-1-0146, and by the Brite EuroMems program, managed by British Aerospace and by Dassault Aviation. Special thanks are due to R.A. Antonia, J. Carlier, R.P. Hoxey, R.D. Moser, A.E. Perry and M. Stanislas for providing their unpublished or hard-to-get data.

References

1. R.A. Antonia, B.R. Pearson: Europhys. Lett. **48**, 163 (1999)
2. R.A. Antonia, M.R. Raupach: Boundary-Layer Meteorol. **65**, 289 (1993)
3. R.F. Blackwelder, H. Eckelmann: J. Fluid Mech. **94**, 577 (1979)
4. K.J. Bullock, R.E. Cooper, F.H. Abernathy: J. Fluid Mech. **88**, 585 (1978)
5. H. Choi, P. Moin, J. Kim: J. Fluid Mech. **262**, 75 (1994)
6. P.G. Drazin, W.H. Reid: *Hydrodynamic Stability* (Cambridge University Press. 1981)
7. T.M. Farabee, M.J. Casarella: Phys. Fluids A **3**, 2410 (1991)
8. H.H. Fernholz, P.J. Finley: Prog. Aerospace Sci. **32**, 245 (1996).
9. M.H. Hites: Scaling of high-Reynolds number turbulent boundary layers in the National Diagnostic Facility. Ph. D. Thesis, Illinois Inst. of Technology (1997)
10. P. Holmes, J.L. Lumley, G. Berkooz: *Turbulence, coherent structures, dynamical systems and symmetry*, (Cambridge Univ. Press. 1996)
11. R.P. Hoxey, P.J. Richards: 'Spectral characteristics of the atmospheric boundary layer near the ground'. In *First UK Wind Engng. Conf. at Cambridge, UK, September 1992*.
12. J.M. Hamilton, J. Kim, F. Waleffe: J. Fluid Mech. **287**, 317 (1995)
13. J. Jeong, F. Hussain, W. Schoppa, J. Kim: J. Fluid Mech. **332**, 185 (1997)
14. J. Jiménez: Phys. Fluids **6**, 944 (1994)
15. J. Jiménez: 'The largest scales of turbulent wall flows'. In *CTR Ann. Res. Briefs*, Stanford Univ. pp. 137–154 (1998)
16. J. Jiménez, P. Moin: J. Fluid Mech. **225**, 213 (1991)
17. J. Jiménez, A. Pinelli: J. Fluid Mech. **389**, 335 (1999)
18. J. Jiménez, M. Uhlmann, A. Pinelli, G. Kawahara: submitted to J. Fluid Mechanics (2000)
19. H.T. Kim, S.J. Kline, W.C. Reynolds: J. Fluid Mech. **50**, 133 (1971)
20. J. Kim, P. Moin, R.D. Moser: J. Fluid Mech. **177**, 133 (1987)
21. K.C. Kim, R.J. Adrian: Phys. Fluids **11**, 417 (1999)
22. M.T. Landahl, E. Mollo–Christensen: *Turbulence and random processes in fluid mechanics* (Cambridge Univ. Press. 1992)
23. C.J. Lawn: J. Fluid Mech. **48**, 477 (1971)
24. M.J. Lee, J. Kim, P. Moin: J. Fluid Mech. **216**, 561 (1990)
25. J.M. Österlund, A.V. Johansson, H.M. Nagib, M.H. Hites: Phys. Fluids **12**, 1 (2000)

26. I. Marusic, J.D. Li, A.E. Perry: 'A study of the Reynolds-shear-stress spectra in zero-pressure-gradient boundary layers'. In *Tenth Australasian Fluid Mech. Conf. at Melbourne, Australia, 11-15 Dec. 1989*. pp. 1.5–1.8.
27. R.D. Moser, J. Kim, N.N. Mansour: Phys. Fluids **11**, 943 (1999)
28. P. Orlandi, J. Jiménez: Phys. Fluids **6**, 634 (1994)
29. A.E. Perry, S. Henbest, M.S. Chong: J. Fluid Mech. **165**, 163 (1986)
30. V.G. Priymak, T. Miyazaki: Phys. Fluids **6**, 3454 (1994)
31. W. Reynolds, W. Tiedermann: J. Fluid Mech. **27**, 253 (1967)
32. S.K. Robinson: Ann. Rev. Fluid Mech. **23**, 601 (1991)
33. C.R. Smith, S.P. Metzler: J. Fluid Mech. **129**, 27 (1983)
34. J.D. Swearingen, R.F. Blackwelder: J. Fluid Mech. **182**, 255 (1987)
35. F. Waleffe: Phys. Fluids **9**, 883 (1997)
36. F. Waleffe: Phys. Rev. Lett. **81**, 4140 (1998)
37. H. Tennekes, J.L. Lumley: *A first course in turbulence* (MIT Press. 1972)
38. S. Toh, T. Itano: preprint, physics/9905012.
39. C.D. Tomkins, Z-C. Lin, R.J. Adrian: Bull. Am. Phys. Soc. **44** (8), 33 (1999)
40. A.A. Townsend: *The structure of turbulent shear flow* (Cambridge U. Press. 1976)
41. M.V. Zagarola, A.J. Smits: Phys. Rev. Lett. **78**, 239 (1997)